Tissue refractive index as marker of disease

Zhuo Wang
Krishnarao Tangella
Andre Balla
Gabriel Popescu

Tissue refractive index as marker of disease

Zhuo Wang,[a] **Krishnarao Tangella,**[b] **Andre Balla,**[c] **and Gabriel Popescu**[a]
[a]University of Illinois at Urbana-Champaign, Beckman Institute for Advanced Science and Technology, Quantitative Light Imaging Laboratory, Department of Electrical and Computer Engineering, Urbana, Illinois 61801
[b]Christie Clinic and University of Illinois at Urbana-Champaign, Department of Pathology, Urbana, Illinois 61801
[c]University of Illinois at Chicago, Department of Pathology, Chicago, Illinois 60612

Abstract. The gold standard in histopathology relies on manual investigation of stained tissue biopsies. A sensitive and quantitative method for *in situ* tissue specimen inspection is highly desirable, as it would allow early disease diagnosis and automatic screening. Here we demonstrate that quantitative phase imaging of entire unstained biopsies has the potential to fulfill this requirement. Our data indicates that the refractive index distribution of histopathology slides, which contains information about the molecular scale organization of tissue, reveals prostate tumors and breast calcifications. These optical maps report on subtle, nanoscale morphological properties of tissues and cells that cannot be recovered by common stains, including hematoxylin and eosin. We found that cancer progression significantly alters the tissue organization, as exhibited by consistently higher refractive index variance in prostate tumors versus normal regions. Furthermore, using the quantitative phase information, we obtained the spatially resolved scattering mean free path and anisotropy factor *g* for entire biopsies and demonstrated their direct correlation with tumor presence. In essence, our results show that the tissue refractive index reports on the nanoscale tissue architecture and, in principle, can be used as an intrinsic marker for cancer diagnosis. © *2011 Society of Photo-Optical Instrumentation Engineers (SPIE)*. [DOI: 10.1117/1.3656732]

Keywords: cancer diagnosis; biopsy imaging; tissue optics; quantitative phase imaging.

Paper 11322R received Jun. 24, 2011; revised manuscript received Sep. 1, 2011; accepted for publication Sep. 22, 2011; published online Nov. 4, 2011.

1 Introduction

Breast cancer and prostate cancer are two of the most widespread cancers in the western world, accounting for approximately 30% of all cases.[1] Following abnormal screening results, a biopsy is performed to establish the existence of cancer and, if present, its grade.[2] The pathologist's assessment of the histological slices represents the definitive diagnosis procedure in cancer pathology and guides initial therapy.[3,4] It is imperative to develop new quantitative methods, combining imaging and computing, capable of assessing biopsies with enhanced objectivity. Such modality, coupled with high-throughput and automatic analysis, will enable pathologists to make more accurate diagnoses more quickly. Toward this end, various label-free techniques have been developed based on both the inelastic (spectroscopic) and elastic (scattering) interaction between light and tissues. Thus, significant progress has been made in near-infrared spectroscopic imaging of tissues.[5–18] On the other hand, light scattering methods operate on the assumption that subtle tissue morphological modifications induced by cancer onset and development are accompanied by changes in the scattering properties and, thus, offer a noninvasive window into pathology.[19–27] Despite these promising efforts, light scattering-based techniques currently have limited use in the clinic. A great challenge is posed by the insufficient knowledge of the tissue optical properties. An ideal measurement will provide the tissue scattering properties over broad spatial scales, which, to our knowledge, remains to be achieved.

In an effort to overcome these limitations, intense efforts have been devoted in recent years toward developing quantitative phase imaging (QPI) methods, where optical path length information across a specimen is quantitatively retrieved (for a review see Refs. 28 and 29). QPI is a label-free approach that has the remarkable ability to render nanoscale morphological information from completely transparent structures with nanoscale pathlength sensitivity.[30–32] It has been shown that the knowledge of the amplitude and phase associated with an optical field transmitted through tissues captures the entire information regarding light-tissue interaction, including scattering properties.[33–36] Yet, the potential of QPI for label-free pathology has not been explored. Here we employ spatial light interference microscopy (SLIM),[37–39] a new white light QPI method developed in our laboratory, to image the entire unstained prostate and breast biopsies and perform a side-by-side comparison with stained pathological slides. Our data demonstrate that the refractive index distribution of tissue is a valuable intrinsic marker of disease and can set the basis for a new generation of computer-assisted, label-free histopathology, to enable earlier disease detection, more accurate diagnosis, and high-sensitivity screening.

2 Results

2.1 Biopsy Imaging Using SLIM

SLIM's principle of operation is described in more detail elsewhere.[37] Briefly, SLIM combines Zernike's phase contrast microscopy[40] with Gabor's holography[41] and yields quantitative optical pathlength maps associated with transparent specimens, including live cells and unstained tissue biopsies. Due to the

Address all correspondence to: Gabriel Popescu, ECE, Beckman Institute, UIUC, 405 North Mathews Avenue, Room 4055, Urbana, Illinois 61801; Tel: 217-333-4840; Fax: (217) 244-1995; E-mail: gpopescu@illinois.edu.
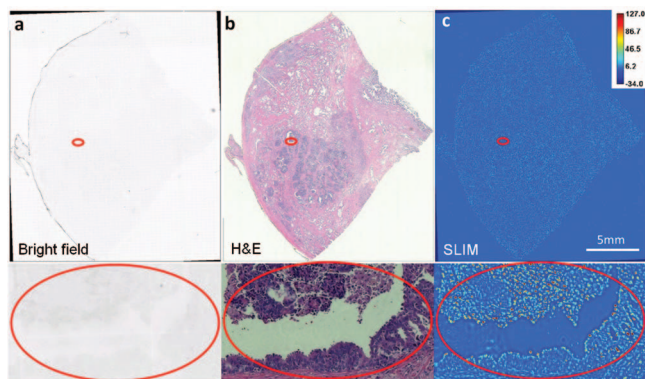
Fig. 1 Multimodal imaging of prostate tissue slices. Objective: 10×/0.3. The field of view is 2.0 cm × 2.4 cm. The size of the blowup (in red circle) is 630 μm × 340 μm. (a) Bright field image of unstained slice (montage of 4131 images). (b) Bright field image of H&E stained slice (montage of 828 images). (c) SLIM phase map of the unstained slice (montage of 4131 images); color bar indicates optical path length in nanometers. Insets show the respective enlarged are indicated as red ellipse.

broadband illumination light[38] and the common-path interferometric geometry, SLIM is highly sensitive to pathlength changes, down to the subnanometer scale.[39]

We implemented SLIM with a programmable scanning stage, which allows for imaging large areas of tissue, up to centimeter scale, by creating a montage of micrometer-resolution images. The number of individual images in the montage depends on the size of the biopsy and varies from several hundred to several thousand. The transverse resolution is limited only by the numerical aperture of the objective and varies in our experiments from 0.4 μm for a 40× (0.75 NA) objective to 1 μm for a 10× (0.3 NA) objective. The spatial pathlength sensitivity of the SLIM images, i.e., the sensitivity to pathlength changes from point to point in the field of view, is remarkably low, approximately 0.3 nm.[37] Since the maximum path-length values are up to the wavelength of light, 530 nm, the signal-to-noise ratio across the image is on the order of 1000.

The specimen preparation is detailed in Sec. 4. Briefly, prostate tissues from patients were fixed with paraffin and sectioned in 4-μm thick slices. Four successive slices were imaged as follows. One unstained slice was deparaffinized and placed in xylene solution for SLIM imaging. The other three slices were deparaffinized and stained with hematoxylin and eosin (H&E), immunohistochemical stained using antibodies against cytokeratin 34 beta E12 (high molecular weight CK903) and alpha methylacyl-CoA-racemase (AMACR), also known as p504s, respectively, and imaged with the same microscope via the bright field channel equipped with a color camera (see Fig. 1 in Ref. 42 for examples of unstained and stained tissue slides).

Figure 1(a) shows the bright field (i.e., common intensity) image of an unstained prostate biopsy. Clearly, little contrast can be observed, which indicates the long-standing motivation for the use of staining in histopathology. The H&E stained slice is shown in Fig. 1(b). The contrast is greatly enhanced as the tissue structures show various shades of color, from dark purple to bright pink. Figure 1(c) shows the optical pathlength map rendered by SLIM, which represents a mosaic of 4131 individual images, with 1 μm transverse resolution. Since the tissue

thickness is known, the SLIM image quantitatively captures the spatial fluctuations of the refractive index. This information fully determines the light-tissue elastic interaction, i.e., its light scattering properties.[34] The refractive index is proportional to the tissue dry mass concentration,[31] which provides complementary information with respect to the dye affinity revealed in common histopathology [Figs. 1(b) and 1(c)].

2.2 Refractive Index Signatures at the Cellular Scale

Both SLIM and stained tissue images were obtained using a 10× (NA = 0.3) objective, which captures multiscale information down to subcellular structures. Figure 2 illustrates the ability of SLIM to reveal particular cell types based on their refractive index signatures. Due to their discoid shape and high refractive index, red blood cells are easily identifiable in the SLIM images [Figs. 2(a) and 2(b)]. Lymphocytes, as evidenced by dark staining in H&E [Fig. 2(d)], were found to exhibit high refractive index in SLIM images [Fig. 2(c)]. The lymphocytes were confirmed by utilizing immunohistochemical stain, namely Leuckocyte Common Antigen (CD45) [Fig. 2(e)]. In a different area of the tissue we found a particular type of cell that seems unlike the rest: while their refractive index is distinctly high, they are sparsely distributed within the tissue [Fig. 2(f)]. In H&E, they show as black dots (see Fig. 2 in Ref. 42). Due to their negative immunostaining for epithelial, myoepithelial, and lymphocytes, these particular cells were identified as stromal. We further use a semiautomatic segmentation program based on IMAGEJ (see Sec. 4) and analyzed the maximal phase value for the three different types of cells. Red blood cells (326), 278 lymphocytes, and 201 stromal cells are identified and analyzed [Fig. 2(g)]. The t-tests of the data show that the significance value (p value) for lymphocyte versus red blood cell and lymphocyte versus stromal cell is essentially zero (3.37×10^{-38} and 4.50×10^{-38}, respectively), while for stromal versus red blood cell, $p = 6.43 \times 10^{-4}$, indicating that the three cell types have their refractive index statistically different. While encouraging, the t-tests results hold little relevance for a small number of cells, when distinguishing among these high-refractive index cells becomes challenging. However, it is possible to take the advantage of the spatial relations, i.e., refractive index correlations, to sort these cells within the biopsy. Note that other cells, e.g., epithelial cells and myoepithelial cells [Fig. 2(a)], relevant for diagnosing prostate cancer, have much lower phases and, thus, can be distinguished quite easily. Therefore, SLIM reveals intrinsic optical properties of cellular and subcellular structures in unstained tissue biopsies. This capability is exploited below in problems of clinical relevance: breast and prostate tissue diagnosis.

2.3 Detection of Microcalcifications in Breast Biopsies

Further, we found interesting optical maps associated with calcifications in the breast. The mammogram is an important screening tool for detecting breast cancer.[43] The presence of abnormal calcifications, i.e., calcium phosphate and calcium oxalate,[44] warrants further work up. Distinguishing between calcium oxalate and calcium phosphate is clinically important. Specifically, it is uncommon for calcium oxalate crystals to be associated with breast malignancy,[45,46] though it can be associated with
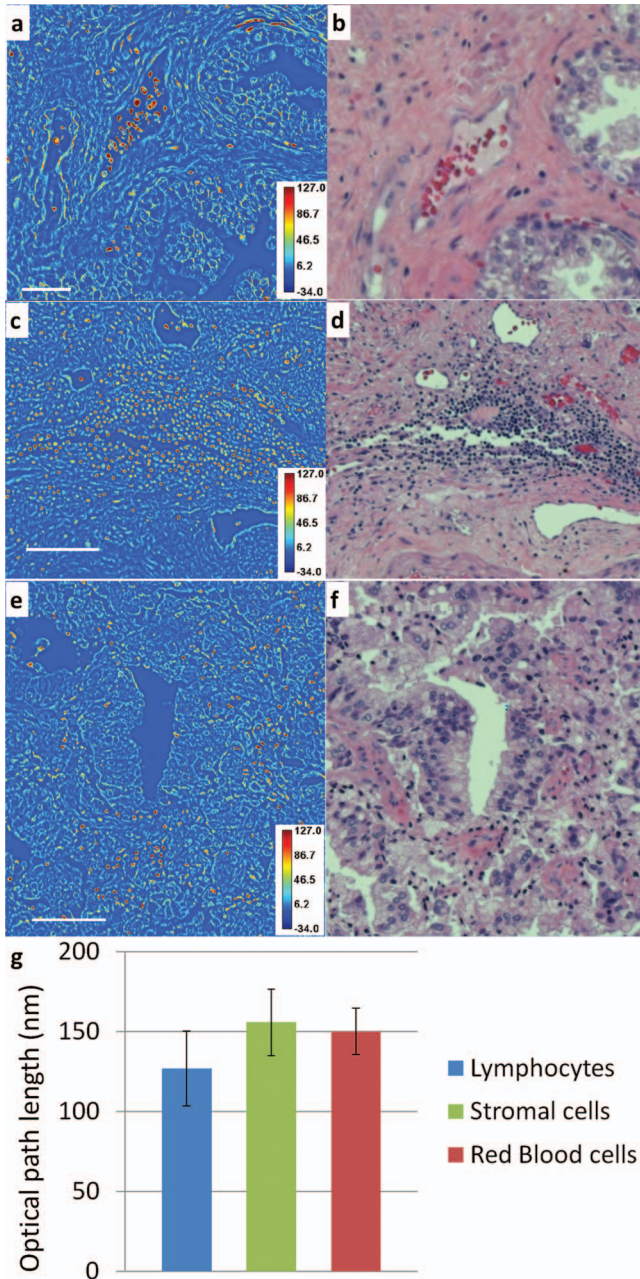
Fig. 2 SLIM imaging signatures. Red blood cells with SLIM (a) and H&E (b). Red blood cells can be identified by their unique shape. Scale bar: 20 μm. Lymphocytes with SLIM (c) and H&E (d). Lymphocytes were confirmed with CD45 staining (see Fig. 2 in Ref. 42). Stromal cells with SLIM (e) and H&E (f). (g) optical path length for the three different cells that feature high refractive index. Scale bar: 100 μm. Color bar indicates optical path length in nanometers.

papillary intraductal carcinoma.[47] Calcium oxalate crystals account for 12% of mammographically localized calcifications that typically prompt for a biopsy procedure.[48] Calcium oxalate is more difficult to detect radiologically and these crystals are easily missed in the biopsies because they do not stain with H&E. These crystals are birefringent and, thus, can be observed in polarized light. However, if the index of suspicion is not high, the pathologist typically does not use polarization microscopy, and calcium oxalate can be missed. The apparent absence of calcification in tissue biopsies reported by the pathologist has a sig-
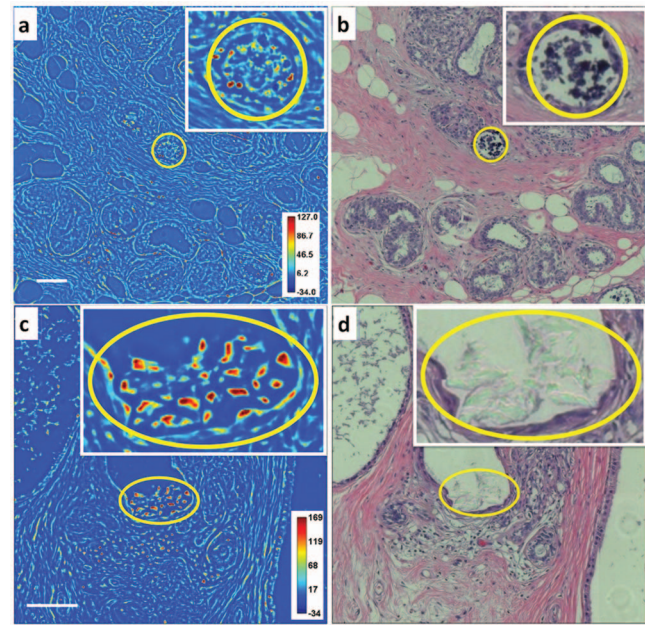

Fig. 3 SLIM imaging of breast microcalcifications. Breast tissue with calcium phosphate: SLIM image (a), color bar in nanometers; H&E image (b). The whole slice is 2.2 cm × 2.4 cm. The SLIM image is stitched by 4785 images and the H&E is stitched by 925 images. Scale bar: 100 μm. Breast tissue with calcium oxalate: SLIM image (c), color bar in nanometers; H&E image (d). The entire slice is 1. 6 cm × 2.4 cm. The SLIM image is stitched by 2840 images and the H&E is stitched by 576 images. Scale bar: 200 μm.

nificant clinical impact, including repeated mammograms and additional, unnecessary surgical intervention.[47,48] Therefore, a consistent means for detecting calcium oxalate is desirable as it decreases significant medical costs and patient anxiety.

Figure 3 illustrates how SLIM may fulfill this challenging task. In Fig. 3(b), the dark H&E staining was identified by pathologists as calcium phosphate. This structure is revealed in the SLIM image as having inhomogeneous refractive index, with a different texture from the surrounding tissue. More importantly, the calcium oxalate crystals are hardly visible in H&E [Fig. 3(d)]; the faint color hues are due to the birefringence of this type of crystal. Clearly, calcium oxalate exhibits a strong refractive index signature, as evidenced by the SLIM image [Fig. 3(c)].

2.4 Refractive Index as Marker for Prostate Cancer

We further studied biopsies from prostate cancer patients. Eleven biopsies from 9 patients were imaged with both SLIM and H&E, as illustrated in Figs. 4(a) and 4(e), respectively (see Sec. 4 for details). For each biopsy, the pathologist identified regions of normal and malignant tissue. From the SLIM image, we computed the map of phase shift variance, $\langle \Delta\phi(\mathbf{r})^2 \rangle$, where the angular brackets denote spatial average (calculated over $32 \times 32 \ \mu m^2$) and $\mathbf{r} = (x, y)$. Figure 4(b) illustrates the map of the scattering mean free path, calculated from the variance as $l_s = L/\langle \Delta\phi(\mathbf{r})^2 \rangle$, as described in Ref. 36. The spatially resolved scattering map shows very good correlation with cancerous and benign areas. It can be easily seen that the regions of high variance, or short scattering mean free path, correspond to the darker staining in H&E, which is associated with the tumor. These
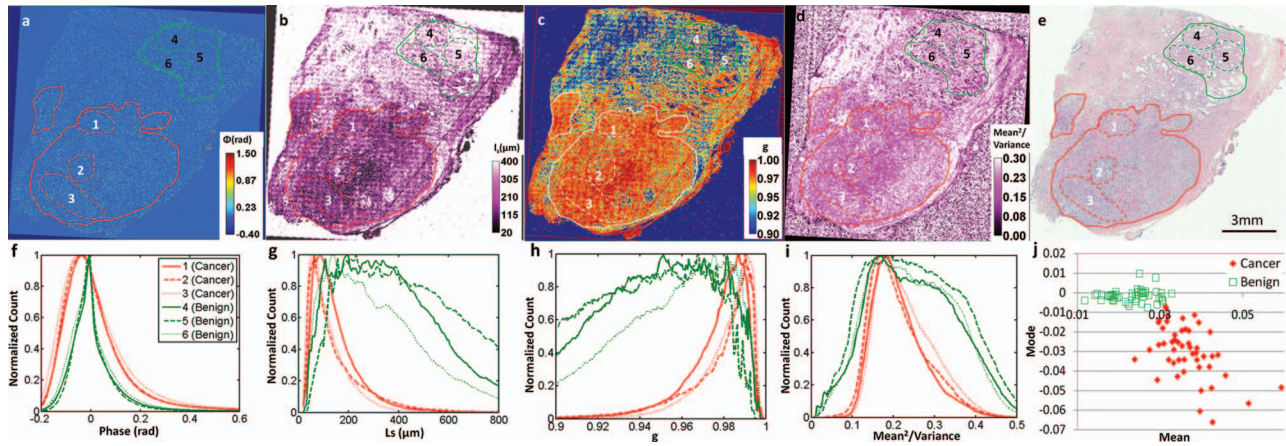
Fig. 4 Multimodal imaging of a prostate tissue biopsy with malignancy; field of view 1.48 cm × 1.44 cm. (a) SLIM unstained slice, color bar indicates optical phase shift in rad. The red lines mark specific cancerous areas (1–3) and the green lines the benign areas (4–6), as identified by the certified pathologist. (b) Scattering mean free path (l_s) map of the tissue slice with the same areas marked. Color bar indicates l_s in micrometers. (c) Anistropic factor g map. (d) Mean square over variance map. (e) H&E stained slice with the same areas marked. (f)–(i). Histograms of the areas in (a)–(d), respectively. (j) Mean versus mode for 49 cancerous areas and 51 benign areas from 11 biopsies.

findings confirm in a direct way the importance of tissue light scattering as a means for cancer diagnosis.[19–27] Essentially, our measurements indicate that prostate cancer renders the tissue more inhomogeneous, which makes it more strongly scattering. These findings are further confirmed by the anisotropy factor measurements [Fig. 4(c)], where malignant areas exhibit consistently higher values of g. These data indicate that cancer affects the tissue architecture in such a way as to render it more inhomogeneous (lower l_s), characterized by angular scattering that is more biased toward the forward direction (higher g). Of course, the absolute values for l_s and g are sensitive to the thickness of the tissue. However, because the refractive index contrast is usually very small, the optical thickness is also very small. Furthermore, cutting errors, if present, are expected to occur at much larger scales than our window used for computation ($32 \times 32 \ \mu m^2$). We seldom observe uneven phase distributions within the same slides covering very large areas of cm^2. Within each slice, the scattering parameter map allows for cancer detection, in which ratios (normal versus cancer) rather than absolute values are of interest. Still, it is possible to introduce some parameters that are independent of the section thickness. One example is the mean squared of the phase divided by the variance [Figs. 4(d) and 4(i)]. This quantity indicates the "contrast" of the refractive index fluctuations.

In order to quantitatively analyze the information contained in the refractive index distribution for the tumor and benign regions, we computed statistical parameters of the first- to fourth-order via the respective histograms. Figures 4(f)–4(i)] show the histograms associated with regions in the maps of Figs. 4(a)–4(d)], respectively. Based on these distributions, we calculated the mean, standard deviation, mode, skewness, and kurtosis for each of the 49 cancer and 51 benign areas [see Fig. 4 in Ref. 42 for various two-dimensional (2D) representations of these parameters]. Unambiguous tumor (red lines) and normal (green lines) regions were selected by a Board Certified pathologist using the H&E slides. The pathologist did not have access to phase images prior to this selection. A second certified pathologist confirmed the classification of the regions in terms of normal versus tumor. As we will show in Sec. 4, we processed many

different parameters and statistics before arriving at the representation of highest separation. Out of the 11 biopsies, 7 were diagnosed by the Board Certified pathologist as Gleason grade 6/10, 2 cases Gleason grade 7/10, 1 case Gleason grade 9/10, and 1 case was benign. With this numerical processing, we generated a multidimensional data space in which we searched for the most confident separation between the two groups of data points. Clearly, as can be seen in Fig. 4 of Ref. 42, all representations show significant separation between the two groups. However, we found that the mode versus mean [Fig. 4(j)] separates the normal from the diseased areas completely from our data set of 100 regions total.

Video 1 illustrates how SLIM might be used in the future for computer assisted diagnosis. The still image shows a frame with the images associated with adenocarcinoma of prostate obtained
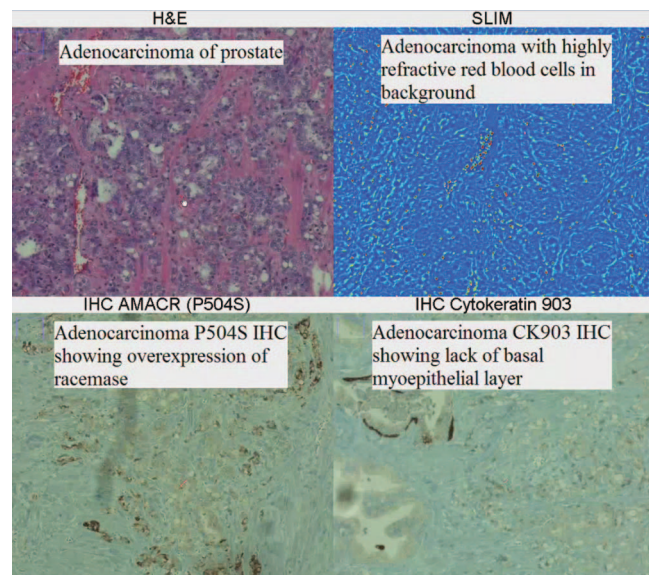
Video 1 Co-registered images obtained by H&E stain, SLIM (label-free), and immonochemical stains, i.e., P504S and CK903, as indicated. (QuickTime, 10.3 MB) [URL: http://dx.doi.org/10.1117/1.3656732.1]

by SLIM and the traditional stains, i.e., H&E and immunochemical stains (P504S and CK903).

3 Summary and Discussion

We showed that, based on the refractive index distribution, SLIM can reveal cellular and subcellular structures in transparent tissue slices. In breast biopsies, the refractive index map identifies microscopic sites of calcifications, which are informative in breast cancer diagnosis and prognosis. The spatial fluctuations of refractive index as captured by the histogram mode, mean, standard deviation, skewness, and kurtosis, strongly correlate with the malignant regions in prostate biopsies. In particular, the 2D representation of mode versus mean looks extremely promising for cancer diagnosis. These initial results warrant further investigation. Current work in our laboratory is dedicated toward expanding our data set and, in the long run, establishing SLIM as a clinical tool.

The prospect of a highly automatic procedure, together with the low cost and high-speed associated with the absence of staining, may make a significant impact in pathology at a global scale. Pathologists are in need of a tool to prescreen slides for areas of concern. Such a tool is already available for pap smears, with improvement in detection rates of individual malignant cells dispersed among thousands of benign cells. It is not difficult to imagine that a high throughput instrument that measures tissue refractive index would be incorporated into the daily activity of pathologists. We can envision a scenario where several unstained slices of tissue will be screened by this technology until something suspicious for malignancy or positive margin of resection is detected. This tool would point out which slices of tissue should be submitted for histology. Further, not all diagnostic and prognostic problems are in the area of established cancer. The method will be especially useful in liver, lung, and colon diseases where incipient fibrosis is an issue.

Finally, it is likely that this type of imaging will impact further the field of optical diagnosis by providing direct access to scattering properties of tissues. Thus, a database of SLIM images associated with various types of tissues, both healthy and diseased, will allow light scattering investigators to look up the scattering mean free path and anisotropy factors of tissues and ultimately predict the outcomes of particular experiments.

4 Methods

4.1 Tissue Preparation

All tissues were handled according to safety regulations by the Institutional Review Board at the University of Illinois and Provena Covenant Medical Center. The tissue used in this procedure was embedded in paraffin and cut on a Leica RM2255 microtome at 4-μm thickness. Seven sequential sections were cut for each specimen block to allow for multimodal imaging. The sections were placed on a water bath at 38 °C. Each section was collected on a separate glass slide making seven sets of slides per specimen. Five of these sets consisted of positively charged glass slides to prevent the tissue from washing off during immunohistochemical staining procedures. The two sets of untreated slides were heat fixed in a 70 °C slide drying oven for 15 min. The slides were then deparaffinized using a routine protocol on a Sakura DRS-601 staining instrument consisting

of two changes of xylene for a total of 3 min, two changes of flex 100 alcohol for a total of 3 min, and two changes in flex 95 alcohol again for a total of 3 min. The slides were then rinsed in distilled water. One set of slides was then dehydrated using the opposite protocol so that the slides finished in two changes of xylene. These slides were then cover-slipped after the dehydration procedure on a tissue-tek cover-slipping instrument using KP-Tape with xylene used as the mounting media. The other set of slides continued through a routine hematoxylin and eosin staining procedure using a Surgipath brand stain system on the same Sakura staining instrument that was used for the deparaffinization process. These slides were then dehydrated and cover-slipped using the same process as the unstained slides.

The immunohistochemical slides were heat fixed in the same 70 °C section drying oven for 30 min. These slides were then deparaffinized and stained on a Ventana Benchmark XT staining instrument using preset protocols defined by Ventana with the following immunohistochemical stains: high molecular weight keratin clone 34betaE12 (also known as cytokeratin 903), leukocyte common antigen clone RP2/18 (also known as CD 45), and P504S clone 13H4 (also known as AMACR), as well as the appropriate previously known positive and species-specific negative controls. After the immunohistochemical staining procedure, the slides were then washed with Dawn liquid dish soap and distilled water to remove the Ventana brand liquid cover-slipping reagent, and then dehydrated and cover-slipped using the same procedure as the two untreated sets of slides used for the unstained and hematoxylin/Eosin stained slides.

4.2 Image Acquisition and Processing

For all the stained images, a 10× objective by ZEISS is used, with lamp power 3200 K, camera exposure setting 0.4 μs, and tile size 872.5 μm × 655.2 μm. For SLIM images, a 10× Ph1 objective by ZEISS is used, with lamp power 3200 K, camera exposure 8 ms, and tile size 388.2 μm by 290.9 μm. The average scanning time for each stained image is 1.4 s, and for each SLIM image is 1.0 s. Our acquisition time varies dramatically with size of the tissue and magnification. A relatively large biopsy imaged with a 10× objective (NA = 0.75) requires ∼4000 images [e.g., Fig. 1(c)]. However, if we scan the same specimen with a 5× objective, the number of images and, thus the total time, drops by a factor of ∼4, for example. The processing time for each phase image is 3.1 s with a desktop equipped with 2.4 GHz Intel Core 2 Duo CPU and 6 GB memory. This number, however, can be significantly improved with a faster imaging and further with parallel computing, as proven recently by our laboratory.[49,50] In principle, QPI can be combined with new technology for tissue scanning, which today is able to scan an entire microscope slide in approximately 1 to 2 min.

A Java-based software plug-in based on IMAGEJ (Ref. 51) was developed to create a montage of the entire biopsy by stitching high-resolution images. As an example, in Fig. 1 the H&E image size is 2.0 × 2.4 cm^2 and is stitched from 828 color images obtained by a 10× objective. Due to 2.25× additional magnification in our SLIM system, 4131 images were used to generate the stitched SLIM images. Then the SLIM images were scaled to the same magnification of H&E, rotated, registered, and cropped to get the accurate overlay as shown. Usually the image size is several gigabytes for both H&E and SLIM stitched images, which

has to be scaled to about 1 to 2 GB for practical handling, storage, and processing. All processing has been performed on a server equipped with 8 CPUs and 20 GB RAM.

4.3 Thickness Independent Parameters

The exact numbers for l_s and g are sensitive to the thickness of the tissue. It is possible to introduce some parameters that are independent to the section thickness. One example is the mean square over variance [Fig. 4(d)]. If we assume L is the tissue thickness, the measured optical path length is thus

$$\phi(x, y, L) = L \times f(x, y), \qquad (1)$$

where $f(x, y) = \frac{2\pi}{\lambda} \frac{1}{L} \int_L \Delta n(x, y, z) dz$ is the normalized phase for section L and Δn is the three-dimensional refractive index contrast. Here we assume f is independent of the section thickness L. The variance of the phase is thus

$$\text{Var}\left[\phi(x, y, L)\right] = L^2 \times \text{Var}\left[f(x, y)\right]. \qquad (2)$$

Since the mean of the phase is

$$\text{Mean}\left[\phi(x, y, L)\right] = L \times \text{Mean}\left[f(x, y)\right], \qquad (3)$$

the mean square over variance is thus

$$\frac{\text{Mean}^2\left[\phi(x, y, L)\right]}{\text{Var}\left[\phi(x, y, L)\right]} = \frac{\text{Mean}^2\left[f(x, y)\right]}{\text{Var}\left[f(x, y)\right]}, \qquad (4)$$

which is independent of the tissue thickness. Similarly, we can define a series of parameters such as Mean cubic over third momentum of the phase ϕ, etc.

It is worth noting that though the thickness of the sections may vary from sample to sample, the thickness of a given section is generally the same within the section. Since it is more important to differ cancer and benign in a specific section, i.e., the ratio is more important than the absolute value, this is not a problem.

4.4 Cell Segmentation

We use a semiautomatic segmentation program based on IMAGEJ and analyzed the maximal phase value for the three different types of cells. Red blood cells (326), 278 lymphocytes, and 201 stromal cells are identified and analyzed. Two sample t-tests (two tailed test, unequal variances) of the data show that the significance value (p value) for red blood cell and lymphocyte 3.37×10^{-38}, for red blood cell and stromal cell 6.43×10^{-4}, and for lymphocyte and stromal 4.50×10^{-38}, meaning they can be differentiated statistically. Other cells such as epithelial cells and myoepithelial cells [Fig. 2(a)] have much lower phases.

References

1. M. J. Walsh and R. Bhargava, "Infrared spectroscopic imaging: an integrative approach to pathology," in *Nanobiophotonics*, G. Popescu, Ed., McGraw-Hill, New York (2010).

2. D. Grignon, P. A. Humphrey, J. R. Srigley, and M. B. Amin, *Gleason Grading of Prostate Cancer: A Contemporary Approach*, Lippincott Williams & Wilkins, Philadelphia (2004).

3. P. A. Humphrey, *Prostate Pathology*, American Society of Clinical Pathology, Chicago (2003).

4. V. Kumar, A. K. Abbas, N. Fausto, S. L. Robbins, and R. S. Cotran, *Robbins and Cotran Pathologic Basis of Disease*, Elsevier Saunders, Philadelphia (2005).

5. J. T. Motz, M. Fitzmaurice, A. Miller, S. J. Gandhi, A. S. Haka, L. H. Galindo, R. R. Dasari, J. R. Kramer, and M. S. Feld, "*In vivo* Raman spectral pathology of human atherosclerosis and vulnerable plaque," *J. Biomed. Opt.* **11**(2), 021003 (2006).

6. R. Bhargava, "Towards a practical Fourier transform infrared chemical imaging protocol for cancer histopathology," *Anal. Bioanal. Chem.* **389**(4), 1155–1169 (2007).

7. W. A. Benalcazar, P. D. Chowdary, Z. Jiang, D. L. Marks, E. J. Chaney, M. Gruebele, and S. A. Boppart, "High-speed nonlinear interferometric vibrational imaging of biological tissue with comparison to Raman microscopy," *IEEE J. Sel. Top. Quantum Electron.* **16**(4), 824–832 (2010).

8. B. Brozek-Pluska, I. Placek, K. Kurczewski, Z. Morawiec, M. Tazbir, and H. Abramczyk, "Breast cancer diagnostics by Raman spectroscopy," *J. Mol. Liq.* **141**(3), 145–148 (2008).

9. P. Crow, B. Barrass, C. Kendall, M. Hart-Prieto, M. Wright, R. Persad, and N. Stone, "The use of Raman spectroscopy to differentiate between different prostatic adenocarcinoma cell lines," *Brit. J. Cancer* **92**(12), 2166–2170 (2005).

10. C. L. Evans, E. O. Potma, M. Puoris'haag, D. Cote, C. P. Lin, and X. S. Xie, "Chemical imaging of tissue *in vivo* with video-rate coherent anti-Stokes Raman scattering microscopy," *Proc. Natl. Acad. Sci. U.S.A.* **102**(46), 16807–16812 (2005).

11. A. S. Haka, K. E. Shafer-Peltier, M. Fitzmaurice, J. Crowe, R. R. Dasari, and M. S. Feld, "Diagnosing breast cancer by using Raman spectroscopy," *Proc. Natl. Acad. Sci. U.S.A.* **102**(35), 12371–12376 (2005).

12. E. B. Hanlon, R. Manoharan, T. W. Koo, K. E. Shafer, J. T. Motz, M. Fitzmaurice, J. R. Kramer, I. Itzkan, R. R. Dasari, and M. S. Feld, "Prospects for *in vivo* Raman spectroscopy," *Phys. Med. Biol.* **45**(2), R1–R59 (2000).

13. C. M. Krishna, N. B. Prathima, R. Malini, B. M. Vadhiraja, R. A. Bhatt, D. J. Fernandes, P. Kushtagi, M. S. Vidyasagar, and V. B. Kartha, "Raman spectroscopy studies for diagnosis of cancers in human uterine cervix," *Vib. Spectrosc.* **41**(1), 136–141 (2006).

14. J. R. Mourant, K. W. Short, S. Carpenter, N. Kunapareddy, L. Coburn, T. M. Powers, and J. P. Freyer, "Biochemical differences in tumorigenic and nontumorigenic cells measured by Raman and infrared spectroscopy," *J. Biomed. Opt.* **10**(3), 031106 (2005).

15. K. E. Shafer-Peltier, A. S. Haka, J. T. Motz, M. Fitzmaurice, R. R. Dasari, and M. S. Feld, "Model-based biological Raman spectral imaging," *J. Cell. Biochem.* **39**, 125–137 (2002).

16. U. Utzinger, D. L. Heintzelman, A. Mahadevan-Jansen, A. Malpica, M. Follen, and R. Richards-Kortum, "Near-infrared Raman spectroscopy for *in vivo* detection of cervical precancers," *Appl. Spectrosc.* **55**(8), 955–959 (2001).

17. H. W. Wang, Y. Fu, T. B. Huff, T. T. Le, H. Wang, and J. X. Cheng, "Chasing lipids in health and diseases by coherent anti-Stokes Raman scattering microscopy," *Vib. Spectrosc.* **50**(1), 160–167 (2009).

18. I. W. Levin and R. Bhargava, "Fourier transform infrared vibrational spectroscopic imaging: Integrating microscopy and molecular recognition," *Ann. Rev. Phys. Chem.* **56**, 429–474 (2005).

19. V. Backman, M. B. Wallace, L. T. Perelman, J. T. Arendt, R. Gurjar, M. G. Muller, Q. Zhang, G. Zonios, E. Kline, J. A. McGilligan, S. Shapshay, T. Valdez, K. Badizadegan, J. M. Crawford, M. Fitzmaurice, S. Kabani, H. S. Levin, M. Seiler, R. R. Dasari, I. Itzkan, J. Van Dam, and M. S. Feld, "Detection of preinvasive cancer cells," *Nature* **406**(6791), 35–36 (2000).

20. I. Itzkan, L. Qiu, H. Fang, M. M. Zaman, E. Vitkin, L. C. Ghiran, S. Salahuddin, M. Modell, C. Andersson, L. M. Kimerer, P. B. Cipolloni, K. H. Lim, S. D. Freedman, I. Bigio, B. P. Sachs, E. B. Hanlon, and L. T. Perelman, "Confocal light absorption and scattering spectroscopic microscopy monitors organelles in live cells with no exogenous labels," *Proc. Natl. Acad. Sci. U.S.A.* **104**(44), 17255–17260 (2007).

21. M. Hunter, V. Backman, G. Popescu, M. Kalashnikov, C. W. Boone, A. Wax, G. Venkatesh, K. Badizadegan, G. D. Stoner, and M. S. Feld, "Tissue self-affinity and light scattering in the Born approximation: A new model for precancer diagnosis," *Phys. Rev. Lett.* **97**, 138102 (2006).

22. L. Qiu, D. K. Pleskow, R. Chuttani, E. Vitkin, J. Leyden, N. Ozden, S. Itani, L. Guo, A. Sacks, J. D. Goldsmith, M. D. Modell, E. B. Hanlon, I. Itzkan, and L. T. Perelman, "Multispectral scanning during endoscopy guides biopsy of dysplasia in Barrett's esophagus," *Nat. Med.* **16**(5), 603–606 (2010).

23. R. A. Drezek, R. Richards-Kortum, M. A. Brewer, M. S. Feld, C. Pitris, A. Ferenczy, M. L. Faupel, and M. Follen, "Optical imaging of the cervix," *Cancer* **98**(9), 2015–2027 (2003).

24. D. A. Benaron, "The future of cancer imaging," *Cancer Metastasis Rev.* **21**(1), 45–78 (2002).

25. R. S. Gurjar, V. Backman, L. T. Perelman, I. Georgakoudi, K. Badizadegan, I. Itzkan, R. R. Dasari, and M. S. Feld, "Imaging human epithelial properties with polarized light-scattering spectroscopy," *Nat. Med.* **7**(11), 1245–1248 (2001).

26. A. Cerussi, D. Hsiang, N. Shah, R. Mehta, A. Durkin, J. Butler, and B. J. Tromberg, "Predicting response to breast cancer neoadjuvant chemotherapy using diffuse optical spectroscopy," *Proc. Natl. Acad. Sci. U.S.A.* **104**(10), 4014–4019 (2007).

27. H. Subramanian, P. Pradhan, Y. Liu, I. R. Capoglu, X. Li, J. D. Rogers, A. Heifetz, D. Kunte, H. K. Roy, A. Taflove, and V. Backman, "Optical methodology for detecting histologically unapparent nanoscale consequences of genetic alterations in biological cells," *Proc. Natl. Acad. Sci. U.S.A.* **105**(51), 20118–20123 (2008).

28. G. Popescu, "Quantitative phase imaging of nanoscale cell structure and dynamics," in *Methods in Cell Biology*, B. P. Jena, Ed., pp. 87–115, Academic Press, San Diego (2008).

29. C. Depeursinge, "Digital holography applied to microscopy," in *Digital Holography and Three-Dimensional Display*, T.-C. Poon, Ed., p. 98, Springer, New York (2006).

30. Y. K. Park, C. A. Best, K. Badizadegan, R. R. Dasari, M. S. Feld, T. Kuriabova, M. L. Henle, A. J. Levine, and G. Popescu, "Measurement of red blood cell mechanics during morphological changes," *Proc. Natl. Acad. Sci. U.S.A.* **107**, 6731–6736 (2010).

31. G. Popescu, Y. Park, N. Lue, C. Best-Popescu, L. Deflores, R. R. Dasari, M. S. Feld, and K. Badizadegan, "Optical imaging of cell mass and growth dynamics," *Am. J. Physiol. Cell. Physiol.* **295**(2), C538–C544 (2008).

32. G. Popescu, T. Ikeda, K. Goda, C. A. Best-Popescu, M. Laposata, S. Manley, R. R. Dasari, K. Badizadegan, and M. S. Feld, "Optical measurement of cell membrane tension," *Phys. Rev. Lett.* **97**, 218101 (2006).

33. N. Lue, J. Bewersdorf, M. D. Lessard, K. Badizadegan, K. Dasari, M. S. Feld, and G. Popescu, "Tissue refractometry using Hilbert phase microscopy," *Opt. Lett.* **32**, 3522–3524 (2007).

34. H. Ding, Z. Wang, F. Nguyen, S. A. Boppart, and G. Popescu, "Fourier transform light scattering of inhomogeneous and dynamic structures," *Phys. Rev. Lett.* **101**, 238102 (2008).

35. H. Ding, F. Nguyen, S. A. Boppart, and G. Popescu, "Optical properties of tissues quantified by Fourier transform light scattering," *Opt. Lett.* **34**, 1372–1374 (2009).

36. Z. Wang, H. Ding, and G. Popescu, "Scattering-phase theorem," *Opt. Lett.* **36**, 1215–1217 (2011).

37. Z. Wang, L. J. Millet, M. Mir, H. Ding, S. Unarunotai, J. A. Rogers, M. U. Gillette, and G. Popescu, "Spatial light interference microscopy (SLIM)," *Opt. Express* **19**(2), 1016–1018 (2011).

38. Z. Wang and G. Popescu, "Quantitative phase imaging with broadband fields," *Appl. Phys. Lett.* **96**, 051117 (2010).

39. Z. Wang, I. S. Chun, X. L. Li, Z. Y. Ong, E. Pop, L. Millet, M. Gillette, and G. Popescu, "Topography and refractometry of nanostructures using spatial light interference microscopy," *Opt. Lett.* **35**(2), 208–210 (2010).

40. F. Zernike, "How I discovered phase contrast," *Science* **121**, 345–349 (1955).

41. D. Gabor, "A new microscopic principle," *Nature* **161**, 777–778 (1948).

42. Z. Wang, K. Tangella, A. Balla, and G. Popescu, "Tissue refractive index as marker of disease: Supplementary figures," http://light.ece.illinois.edu/JBO_TissueRefractive_supp.pdf (2011).

43. H. D. Nelson, K. Tyne, A. Naik, C. Bougatsos, B. K. Chan, and L. Humphrey, "Screening for breast cancer: an update for the U.S. Preventive Services Task Force," *Ann. Intern. Med.* **151**(10), 727–737, W237–W242 (2009).

44. G. M. Tse, P. H. Tan, A. L. Pang, A. P. Tang, and H. S. Cheung, "Calcification in breast lesions: pathologists' perspective," *J. Clin. Pathol.* **61**(2), 145–151 (2008).

45. L. Frappart, I. Remy, H. C. Lin, A. Bremond, D. Raudrant, B. Grousson, and J. L. Vauzelle, "Different types of microcalcifications observed in breast pathology–correlations with histopathological diagnosis and radiological examination of operative specimens," *Virchows Arch, A* **410**(3), 179–187 (1986).

46. J. E. G. Gonzalez, R. G. Caldwell, and J. Valaitis, "Calcium-oxalate crystals in the breast–pathology and significance," *Am. J. Surg. Pathol.* **15**(6), 586–591 (1991).

47. N. Singh and J. M. Theaker, "Calcium oxalate crystals (Weddellite) within the secretions of ductal carcinoma in situ–a rare phenomenon," *J. Clin. Pathol.* **52**(2), 145–146 (1999).

48. L. D. Truong, J. Cartwright, and L. Alpert, "Calcium-oxalate in breast-lesions biopsied for calcification detected in screening mammography - incidence and clinical-significance," *Mod. Pathol.* **5**(2), 146–152 (1992).

49. H. Pham, N. Ding, N. Sobh, M. Do, S. Patel, and G. Popescu, "Off-axis quantitative phase imaging processing using CUDA: toward real-time applications," *Biomed. Opt. Express* **2**, 1781–1793 (2011).

50. H. F. Ding and G. Popescu, "Instantaneous spatial light interference microscopy," *Opt. Express* **18**(2), 1569–1575 (2010).

51. W. S. Rasband, "IMAGEJ," U.S. National Institutes of Health, Bethesda, Maryland, USA, http://rsb.info.nih.gov/ij/ (1997 to 2009).